



The structure of lipid nanodisc-reconstituted TRPV3 reveals the gating mechanism

Hiroto Shimada^{1,5}, Tsukasa Kusakizako^{1,5}, T. H. Dung Nguyen², Tomohiro Nishizawa¹, Tomoya Hino^{1,3,4}, Makoto Tominaga^{1,2} and Osamu Nureki¹✉

Transient receptor potential vanilloid subfamily member 3 (TRPV3) is a temperature-sensitive cation channel. Previous cryo-EM analyses of TRPV3 in detergent micelles or amphipol proposed that the lower gate opens by α -to- π helical transitions of the nearby S6 helix. However, it remains unclear how physiological lipids are involved in the TRPV3 activation. Here we determined the apo state structure of mouse (*Mus musculus*) TRPV3 in a lipid nanodisc at 3.3 Å resolution. The structure revealed that lipids bound to the pore domain stabilize the selectivity filter in the narrow state, suggesting that the selectivity filter of TRPV3 affects cation permeation. When the lower gate is closed in nanodisc-reconstituted TRPV3, the S6 helix adopts the π -helical conformation without agonist- or heat-sensitization, potentially stabilized by putative intra-subunit hydrogen bonds and lipid binding. Our findings provide insights into the lipid-associated gating mechanism of TRPV3.

Transient receptor potential (TRP) channels are nonselective cation channels responding to physical or chemical stimuli¹.

The TRPV family, one of the TRP superfamilies, consists of TRPV1–TRPV6. TRPV1–TRPV4 are categorized as thermoTRP channels, responding to thermal stimuli, while TRPV3 responds to innocuous temperatures (33 °C)^{2,3} or chemical compounds, such as camphor, carvacrol and 2-aminoethoxydiphenyl borate (2-APB), and permeates cations nonselectively^{4–6}. TRPV3 is expressed mainly in keratinocytes and is thought to contribute to the skin barrier. TRPV3 is related to human skin diseases, including Olmsted syndrome and atopic dermatitis^{7–10}.

As the activation temperature of TRPV3 varies with the composition of the lipid bilayer, lipids are considered to be involved in TRPV3 activation. Cholesterol lowers the activation temperature of TRPV3 (ref. ¹¹). Unsaturated fatty acids directly activate TRPV3 (ref. ¹²), whereas phosphatidylinositol 4,5-bisphosphate inhibits activation¹³. Cryogenic electron microscopy (cryo-EM) structures of TRPV1 in nanodiscs visualized the specific binding of the phospholipid in the vanilloid-binding pocket and suggested that the temperature-dependent lipid displacement induces the channel opening of TRPV1 (ref. ¹⁴).

Recent cryo-EM analyses of TRPV channels suggested that TRPV1 and TRPV2 have two, upper and lower, gates^{15–17}. In contrast, TRPV3 has the constitutively conducting selectivity filter, which is similar in all of the reported structures, and thus the selectivity filter is considered to be nonfunctional as the upper gate^{18–20}. Singh et al. determined the structures of TRPV3 in the closed and open states, and the middle of the S6 helix adopts π -helical conformation only in the open state. The structural comparison suggested that the S6 helix undergoes α -to- π helical transitions during the lower gate opening of TRPV3 (ref. ¹⁸). TRPV3 becomes sensitized on repeated stimulation with either heat or agonists^{5,12,21}. Zubcevic et al. analyzed the sensitized state structure produced by a treatment with 2-APB¹⁹, and found that the S6 helix adopts the π -helical conformation, while the lower gate is closed. This sensitized state is

speculated to represent a closed state that has a lower energy barrier for channel opening¹⁹. More recently, Singh et al. reported the structures of TRPV3 in temperature-activated sensitized and open states, suggesting that intracellular rearrangement induces the opening of the pore domain²². However, it remains unclear how lipids are involved in the TRPV3 activation, due to the lack of structural information for TRPV3 reconstituted in a lipid bilayer.

In this study, we determined the apo state structure of mouse TRPV3 in a lipid nanodisc at 3.3 Å resolution, revealing the lipid–protein interaction in TRPV3. The bound lipid stabilized the selectivity filter of TRPV3 in a narrow state, indicating that the lipids are involved in stabilizing the narrow state of the selectivity filter. The S6 helix adopts the π -helical conformation in the middle portion, stabilized by hydrogen bonds and lipid interactions. We propose the lipid-associated gating mechanism of TRPV3, based on the structure of TRPV3 in a nanodisc.

Results

Structure determination of TRPV3 in a nanodisc. We performed cryo-EM single-particle analysis of the lipid nanodisc-reconstituted TRPV3, to elucidate the lipid-associated activation mechanism. For the structural analysis, we selected mouse (*M. musculus*) TRPV3 (mTRPV3), which was previously used for electrophysiological studies^{5,23,24} and structural studies^{18,22}, and the N-terminal 1–117 residues were truncated to improve molecular stability. To confirm the function of this truncated mutant (mTRPV3-ΔN), we performed the electrophysiological analysis using human embryonic kidney 293 (HEK293) cells expressing mTRPV3-ΔN, showing that this truncated mutant responded at 50 °C, similar to the full-length channel²³. The camphor or 2-APB evoked current per unit capacitance of mTRPV3-ΔN is almost the same as that of full-length wild-type mouse TRPV3 (Extended Data Fig. 1a–c).

The purified mTRPV3-ΔN was reconstituted into a nanodisc²⁵ (Extended Data Fig. 1d,e), consisting of soybean phosphatidylcholine and MSP2N2, which has a diameter of ~150 Å and was

¹Department of Biological Sciences, Graduate School of Science, The University of Tokyo, Bunkyo-ku, Tokyo, Japan. ²Division of Cell Signaling, National Institute for Physiological Sciences, National Institute of Natural Sciences, Okazaki, Japan. ³Department of Chemistry and Biotechnology, Graduate School of Engineering, Tottori University, Tottori, Japan. ⁴Center for Research on Green Sustainable Chemistry, Tottori University, Tottori, Japan. ⁵These authors contributed equally: Hiroto Shimada, Tsukasa Kusakizako. ✉e-mail: nureki@bs.s.u-tokyo.ac.jp

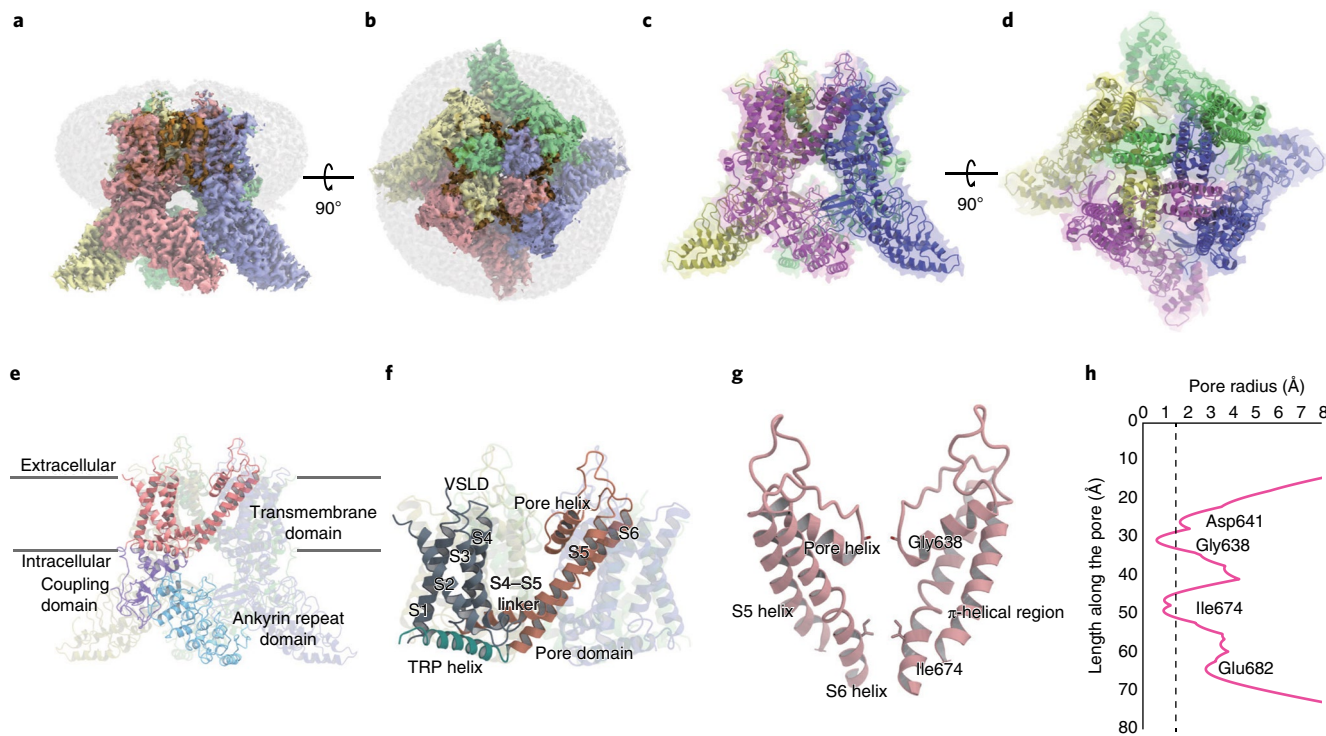


Fig. 1 | Architecture and ion permeation pore of mouse TRPV3 (mTRPV3- Δ N) in a lipid nanodisc. **a,b**, Side (**a**) and top (**b**) views of the three-dimensional cryo-EM reconstruction of the mTRPV3- Δ N tetramer in a lipid nanodisc, colored by protomer (red, blue, green and yellow). The lipid-occupied site is colored brown. **c,d**, Side (**c**) and top (**d**) views of the atomic model of the tetrameric mTRPV3- Δ N in ribbons, in the same orientation and colors as the density map in **a** and **b**. **e**, Overview of the structural elements within a single protomer of the TRPV3 channel: the ARD is blue, the coupling domain is purple and the transmembrane domain, including the TRP helix and S1-S6 helices, is pink. **f**, Architecture of the transmembrane domain within a single protomer of the TRPV3 channel: the voltage sensing-like domain (VSLD), containing S1-S4, is colored gray; in the pore domain, including the S4-S5 linker and S5-S6 helices, the pore helix is orange and the TRP helix is green. **g**, The residues lining the pathway in two opposing monomers of mTRPV3- Δ N in a nanodisc. **h**, The pore radius of mTRPV3- Δ N in a nanodisc. The vertical dashed line denotes the radius of a water molecule, 1.4 Å.

previously used for cryo-EM analyses of TRP channels^{14,26–28}. We first prepared vitrified samples of nanodisc-reconstituted mTRPV3- Δ N, but the cryo-EM images of these samples showed aggregated particles. To protect the particles from aggregation, we added digitonin at a final concentration of 0.01% (lower than its critical micelle concentration value) to the nanodisc-reconstituted mTRPV3- Δ N sample just before vitrification, resulting in the improved distribution of nanodisc-reconstituted mTRPV3- Δ N.

We collected 1,817 cryo-EM images of mTRPV3- Δ N in a nanodisc (Extended Data Fig. 2). The two-dimensional class averaged maps showed that mTRPV3- Δ N was properly reconstituted in the disk-shaped lipid bilayer, similar to other TRP channels embedded in nanodiscs. Three-dimensional refinement with the imposed C4-symmetry revealed the apo state structure of mTRPV3- Δ N in a nanodisc at ~3.3 Å resolution (Fig. 1a,b, Table 1 and Extended Data Fig. 2d,f). The local resolution was better in the transmembrane domain (~2.9 Å resolution) as compared to the intracellular domain (Extended Data Fig. 3). The whole density map was sufficient to define the side chains (Extended Data Fig. 4), and the Arg118–Arg464 and Leu482–Ile756 residues were modeled into the density (Fig. 1c,d).

The overall structure and channel pore. TRPV3 in a nanodisc has the typical architecture of other TRP channels (Fig. 1c,d), composed of three domains, the N-terminal ankyrin repeat domain (ARD), the transmembrane domain consisting of six transmembrane helices (S1–S6) and the coupling domain consisting of the TRP helix and the C-terminal β -strands (Fig. 1e). The transmembrane domain has domain-swapped architecture, in which the S1–S4 helical bundle

called a voltage sensing-like domain surrounds the central pore domain, consisting of S5–S6 helices and the intervening pore helix (Fig. 1d,f). Arg464–Leu482 located on the loop between the S1–S2 helices were not modeled due to the poor density of the map, indicating the conformational flexibility of this loop.

Notably, there are seven lipid-like densities (lipids 1–7) embedded at the tetramer interface and surrounding the channel helices (S5–S6 helices and the pore helix) (Fig. 1a and Extended Data Fig. 5a). Among them, we identified five densities with strong (2.4 σ) bifurcated acyl-chain-like characteristics. We assumed that these lipid-like densities are phosphatidylcholine (PC) because we used PC lipids from soybean for the nanodisc reconstitution and modeled PC into these densities. The other two robust nonprotein densities (lipids 6 and 7) are not bifurcated acyl-chain-like densities, and thus we modeled parts of the acyl chains into the observed densities (Extended Data Fig. 5a). Lipids 1, 2 and 6 are located at positions similar to the previously reported structures. Lipid 1 is bound to a vanilloid-binding pocket presumably associated with TRPV1 activation¹⁴ (Extended Data Fig. 5b). Lipids 2 and 6 were also observed in the apo state TRPV3 structure in digitonin micelles (Protein Data Bank (PDB) ID 6DVW)¹⁸ (Extended Data Fig. 5c,d). Lipids 2 and 6 are located between the S3 and S6 helices and among the S1, S2 and TRP helices, respectively¹⁸ (Extended Data Fig. 5c,d). By contrast, the remaining four lipids (lipids 3, 4, 5 and 7) are newly identified in the current nanodisc structure (discussed in the sections Architecture of the selectivity filter of TRPV3 and Stabilization of the π -helix in S6).

Similar to the previously reported TRPV3 structures, the pore of TRPV3 in a nanodisc is lined by the four-fold symmetric pore

Table 1 | Data collection, refinement and validation statistics

TRPV3 in nanodisc (EMD-0882, PDB 6LGP)	
Data collection and processing	
Magnification (nominal)	×96,000
Voltage (kV)	300
Electron exposure (e ⁻ /Å ²)	50
Defocus range (μm)	−0.5 to −2.5
Pixel size (Å)	0.8346
Symmetry imposed	C ₄
Initial particle images (no.)	469,323
Final particle images (no.)	106,937
Map resolution (Å)	3.314
FSC threshold	0.143
Map resolution range (Å)	2.6–4.2
Refinement	
Model resolution (Å)	3.35
FSC threshold	0.5
Map sharpening B factor (Å ²)	−62.1
Model composition	
Nonhydrogen atoms	21,212
Protein residues	20,244
Ligands	968
B factors (Å ²)	
Protein	61.78
Ligand	57.68
R.m.s. deviations	
Bond lengths (Å)	0.008
Bond angles (°)	0.775
Validation	
MolProbity score	2.05
Clashscore	8.51
Poor rotamers (%)	0.0
Ramachandran plot	
Favored (%)	88.1
Allowed (%)	11.7
Disallowed (%)	0.2

domains (Fig. 1d,g). Using the HOLE program²⁹, we calculated the van der Waals radii of the ion conduction pathway (Fig. 1h), revealing that the apo state structure of TRPV3 in a nanodisc has two constriction sites along the channel pore. The upper constriction site is formed by the backbone carbonyls of Gly638 (0.61 Å radius) located on the pore loop. The lower constriction site is formed by the side chain of Ile674 (0.92 Å radius), located in the middle of the S6 helix. These constrictions are narrow enough to prevent hydrated cation permeation, and thus our apo state structure of TRPV3 in a nanodisc represents a closed state.

Architecture of the selectivity filter in TRPV3. The selectivity filter of TRPV3 is defined by the residues G⁶³⁸LGD⁶⁴¹ (Supplementary Fig. 1), and the two glycine residues and aspartic acid residue are highly conserved among the heat-sensitive TRPV family members. In the present TRPV3 structure in a nanodisc, these residues are located between the pore helix and S6 helix, and the constriction

site is composed of the diagonally opposed carbonyl oxygen atoms of Gly638 (Fig. 2a and Extended Data Fig. 6a), as also observed in the TRPV1–TRPV4 structures (Gly643 in TRPV1, Gly605 in TRPV2, Gly675 in TRPV4)^{14,16,17,30}. The distance between the carbonyl oxygen atoms of Gly638 is 4.5 Å, which is too narrow to permeate hydrated cations such as Na⁺, K⁺ and Ca²⁺, with 6–9 Å diameters^{31–33}, and is about 2.2–2.6 Å closer than those in all of the previously reported TRPV3 structures (Fig. 2a)^{18–20}. Thus, the selectivity filter of the current structure is likely to represent a narrow state. Therefore, contrary to the conventional model, the selectivity filter of TRPV3 is implicated in channel gating. The structural comparison with the sensitized state structure of TRPV3 (PDB 6MHS) indicated that the pore helix undergoes a clockwise rotation by about 9°, as viewed from the extracellular side, relative to the present structure of TRPV3 in a nanodisc (Fig. 2b and Extended Data Fig. 6b). In addition, accompanying this rotation, the backbone carbonyl group of Gly638 points away from the central pore (Fig. 2c). These observations suggest that the widening of the selectivity filter is associated with the rotation of the pore helix and the consequent separation of the carbonyl oxygen of Gly638.

In the present structure of TRPV3 in a nanodisc, we newly identified a phosphatidylcholine molecule (lipid 3), bound between the S6 helix and the pore helix (Fig. 2d). The phosphatidylcholine acyl chains penetrate the space between these helices and associate with the hydrophobic residues, such as Leu630, Phe633 and Ile637 of the pore helix, and Leu655 and Phe656 of the S6 helix (Fig. 2d). Lipid 3 densities were not observed in the previously reported conducting state structures, and the structural comparison indicated that lipid 3 sterically interferes with the selectivity filter in the conducting state (PDB 6MHS), because the side chains of Leu630, Phe633 and Phe626 on the pore helix occupy the binding site of lipid 3 (Fig. 2e and Extended Data Fig. 6c). These observations suggest that lipid 3 stabilizes the selectivity filter in the narrow state.

TRPV1 and TRPV2 have an additional constriction site located on the extracellular side of the selectivity filter, composed of the sulfur atoms of methionine (Met644 in TRPV1 and Met606 in TRPV2)^{16,17} (Fig. 2f,g). While this methionine residue is conserved in other heat-sensitive TRPV family members (TRPV1, 2 and 4), it is replaced with leucine in TRPV3 (Supplementary Fig. 1). The side chain of the corresponding Leu639 points away from the central pore axis and does not form any constriction site (Fig. 2h). Consequently, the upper constriction site of TRPV3 is essentially composed of the carbonyl oxygens of Gly638. This difference may explain the higher channel conductance of TRPV3 (174 pS)³⁴, as compared to other heat-sensitive TRPV family members.

The lower gate architecture of TRPV3. The Ile674 residue in the S6 helix constitutes the lower gate constriction. The van der Waals radius of the conduction pore is 0.92 Å and insufficient to permeate hydrated cations (Figs. 1h and 3a). While Ile674 similarly constitutes the lower gate in the previous structures of the sensitized and open states of TRPV3, Met677 forms the lower gate in the closed apo state of TRPV3 (Fig. 3b–e and Extended Data Fig. 6d–g). These structures suggested that the opening of the lower gate is associated with the α- to π-helix transition in the middle portion of the S6 helix. However, in the present structure of TRPV3 in a nanodisc, Phe666–Leu670 form a π helix near the lower gate (Fig. 3f), while Ile674 still constitutes the closed lower gate constriction (hereafter referred as the ‘closed-π state’). The current closed-π state structure of TRPV3 in a nanodisc suggests that the S6 helix can form a π-helix in the lipid bilayer, even without agonist- or heat-induced sensitization.

Stabilization of the π-helix in S6. The closed-π state of TRPV3 is characterized by a hydrogen bond between the side chains of Asp586 on the S5 helix and Thr680 on the S6 helix in the same

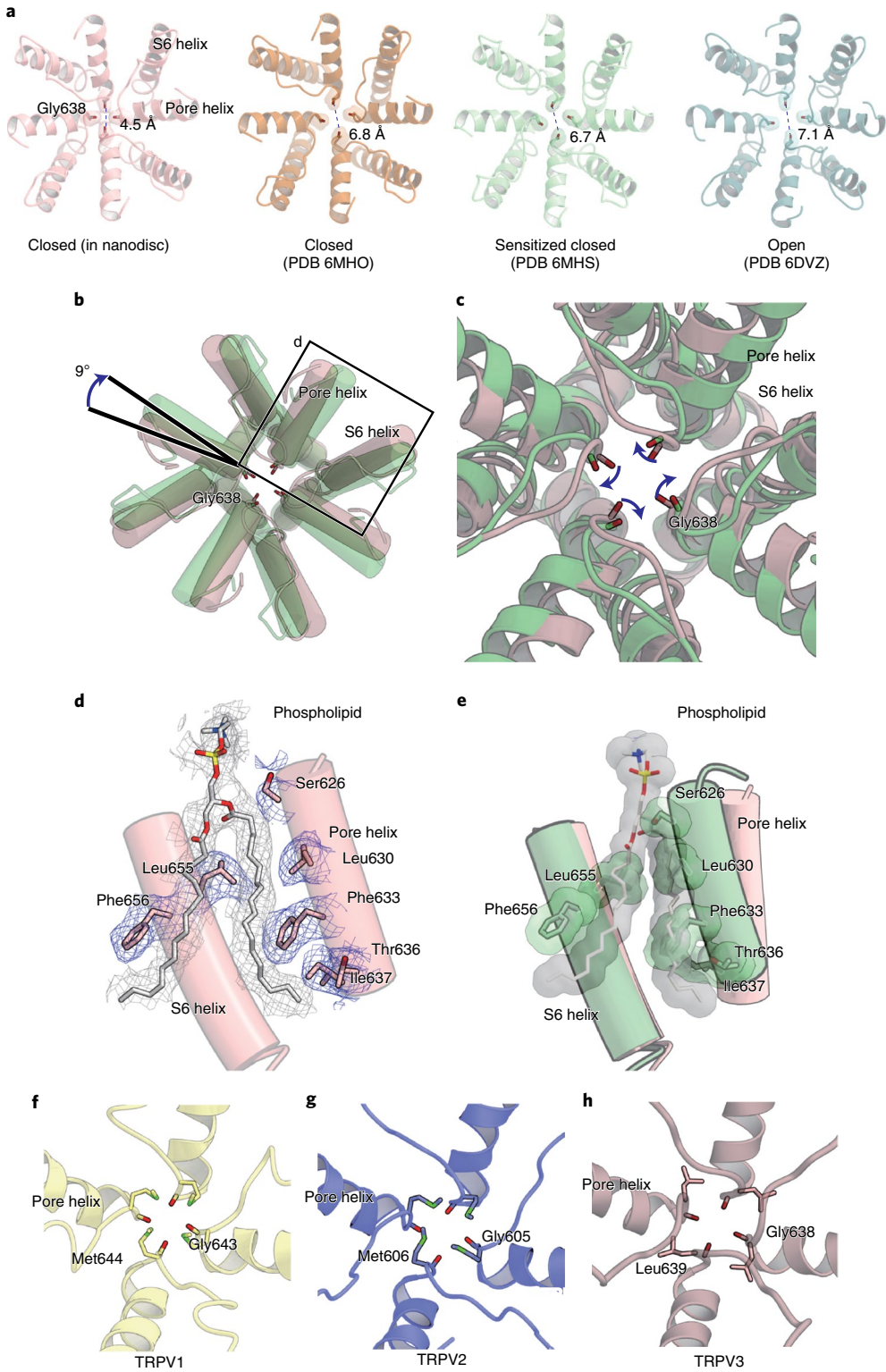


Fig. 2 | Structural changes of the selectivity filter in TRPV3. **a**, Comparison of the extracellular views of the pore domain among TRPV3 states. Closed in nanodisc, pink; closed state (PDB 6MHO), orange; sensitized state (PDB 6MHS), light green and open structure (PDB 6DVZ), cyan. The opposed backbone carbonyls of Gly638 are shown in Corey-Pauling-Koltun (CPK) and stick models. **b**, Superimposition of the pore domains of TRPV3 in a nanodisc (pink) and the TRPV3-sensitized state (green), according to the C α of the S6 helices (Pro651-Ser685), viewed extracellularly. **c**, Detailed view of the selectivity filters of TRPV3 in a nanodisc (pink) and the TRPV3-sensitized state (green). **d**, Phospholipid-binding site between the S6 helix and pore helix (boxed region in **b**). The phospholipid and the interacting residues are indicated by stick models. The density map of the phospholipid is shown in gray, and that of the residues is shown in navy blue. **e**, Comparison between the phospholipid-binding site in **d** in TRPV3 in a nanodisc (pink) and in the TRPV3-sensitized state (green). Both models are superimposed on the C α of the S6 helices (Pro651-Ser685) as a guide. The phospholipid observed in a nanodisc and the same residues indicated in **d** in the sensitized state are indicated by stick and CPK models, showing that the residues clashed with lipid 3. **f-h**, Comparison of the selectivity filter components in TRPV1 (**f**), TRPV2 (**g**) and TRPV3 (**h**), viewed from the extracellular side. TRPV1 (**f**) (PDB 5IRZ) and TRPV2 (**g**) (PDB 5AN8) have the methionine upper gate, while in TRPV3 (**h**), the opposed carbonyl oxygen of Gly638 is directly exposed to the extracellular surface.

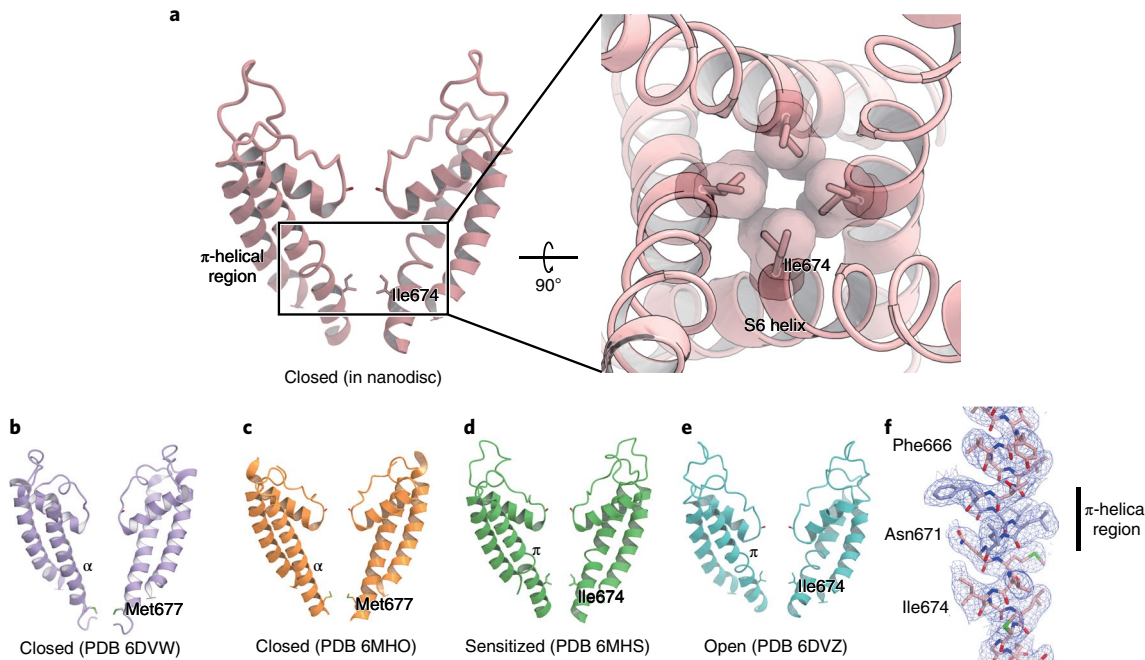


Fig. 3 | Lower gate architecture of TRPV3 in a nanodisc. **a**, Side (left) and top (right) views of the pore domain of TRPV3 in a nanodisc (**a**). The van der Waals surface of Ile674 is shown in the top view. The apo state of TRPV3 in a nanodisc has the π -helical region in the S6 helix, and the residue facing the lower constriction site is Ile674. **b–e**, Comparison of the lower gates in TRPV3 in the closed state in digitonin micelles (lilac) (**b**), the closed state in amphiphilic (orange) (**c**), the sensitized state (green) (**d**) and the open state (light blue) (**e**). The apo state of TRPV3 in a nanodisc has a similar architecture to the TRPV3-sensitized state. **f**, The details of the π -helical region of TRPV3 in a nanodisc. The model of TRPV3 in a nanodisc is shown as a stick model, with the π -helical region colored blue. The cryo-EM density is shown by a navy mesh (2.5 σ).

subunit (Fig. 4a). The electron microscopy potential map of TRPV3 in a nanodisc lacks sufficient resolution to identify hydrogen bonds. However, the densities of the S5 and S6 helices are clear (with the higher local resolution of about 2.9 Å) (Extended Data Fig. 4i), which suggested the putative hydrogen bond formation between these residues (Fig. 4b). In the previous TRPV3 structures, a similar hydrogen bond interaction is observed only in the open state (Fig. 4b), suggesting that it stabilizes the open channel pore¹⁸. Therefore, the hydrogen bonding formation in the current closed- π structure conflicts with this view. To examine the effect of the hydrogen bonding between Asp586-Thr680 on channel gating, we performed whole-cell patch-clamp analyses (Fig. 4c–e). HEK293 cells expressing the T680A mutant showed no detectable currents on either agonist (camphor or 2-APB) or heat stimulation, although this mutant was present on the plasma membrane (Fig. 4f). The electrophysiological results of the T680A mutant revealed that Thr680 is critical for channel gating, through a mechanism that might potentially include hydrogen bonding. A structural comparison among the closed- π state structures of TRPV family members demonstrated that a similar suggested hydrogen bond is also observed in the closed state structure of TRPV1, between Asp576-Thr685 (Fig. 4b). These Asp and Thr residues are conserved among TRPV1–TRPV4 (Supplementary Fig. 1). Therefore, this hydrogen bond is probably involved in the channel gating in TRPV1–TRPV4. Taken together with the previous studies, TRPV3 is likely to adopt the closed- π state, rather than the closed- α state, in the lipid bilayer. The hydrogen bond between Asp586-Thr680 is probably important for maintaining the π -helix configuration of S6 during the stimuli-induced structural transition from the closed- π to open state.

Discussion

In this study, we determined the cryo-EM structure of TRPV3 in a nanodisc at 3.3 Å resolution, providing insights into the molecular

mechanism of TRPV3 in lipid bilayers (Fig. 5). Previous studies suggested that the cation-permeable selectivity filter of TRPV3 is nonfunctional as the upper gate^{18,19}, but our structure of TRPV3 in a nanodisc opposes this view and indicates that the selectivity filter of TRPV3 is important for the channel activation. A recent study showed that thiol-reactive ions can pass the selectivity filters in TRPV3 channels in the absence of activating stimuli, suggesting that the selectivity filter of TRPV1–TRPV3 is not an activation gate³⁵. As discussed herein, the selectivity filter is in equilibrium between the narrow and wide states, and the gating equilibrium of the selectivity filter is shifted toward the narrow state in the absence of stimuli. Based on the present structure, the selectivity filter in the narrow state (0.61 Å radius, Fig. 1h) cannot allow the passage of thiol-reactive ions, such as Ag⁺ (1.15 Å radius). Thus, the thiol-reactive ions may permeate the wide state selectivity filter in the conformational equilibrium. Furthermore, our nanodisc structure identified the phospholipid bound between the S6 and pore helices that stabilizes the narrow state of the selectivity filter, suggesting that the lipid dissociation is involved in the widening of the selectivity filter (Fig. 5a).

The current closed state structure of TRPV3 in a nanodisc adopts the π -helical conformation in the middle portion of the S6 helix, even without agonist binding (Fig. 5b). The electrophysiological analysis suggested that the hydrogen bond between Asp586 and Thr680 is important for maintaining the π -helical region during channel activation. We newly identified three lipids around Asp586 in the S5 helix (lipids 4, 5 and 7) (Extended Data Fig. 7a). The extracellular and intracellular sides of S5 form hydrophobic interactions with the acyl chains of lipids 4 and 7, respectively (Extended Data Fig. 7b,c). These lipids probably stabilize the S5 helix, by forming hydrophobic interactions (Extended Data Fig. 7b,c). The density corresponding to lipid 7 is also observed in both the sensitized state (PDB 6MHS) (Extended Data Fig. 7d) and the open state (PDB

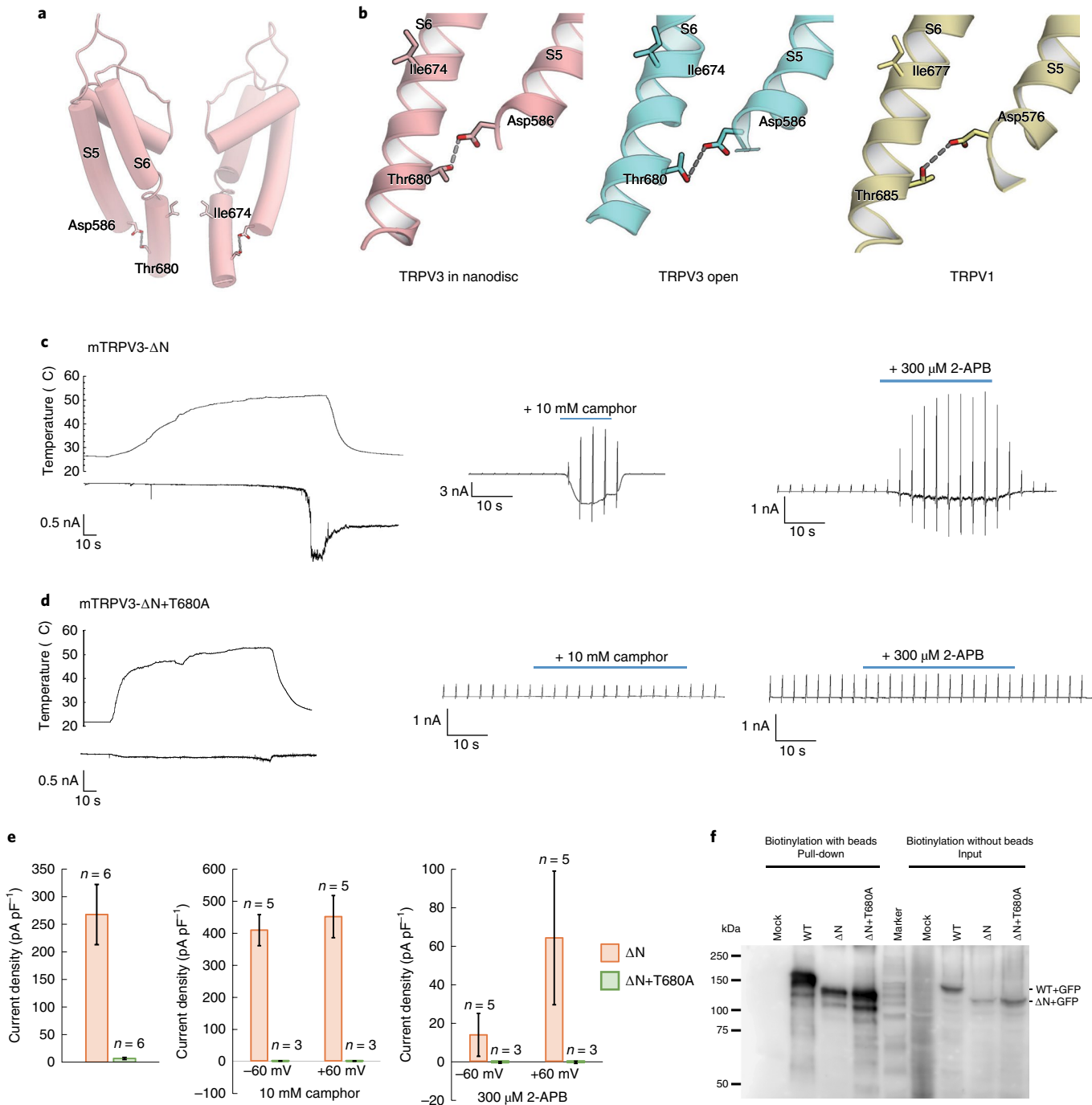


Fig. 4 | The hydrogen bond between Asp586 and Thr680. **a**, Side view of the pore domain of TRPV3 in a nanodisc, including S5, S6 and pore helices. **b**, Close-up view of Asp586-Thr680 in the closed state structure of TRPV3 in a nanodisc (left), Asp586-Thr680 in the open state structure of TRPV3 (center) and Asp576-Thr685 in the closed state structure of TRPV1 in a nanodisc (right). **c,d**, Whole-cell patch-clamp recordings in HEK293 cells expressing mTRPV3-ΔN (**c**) or mTRPV3-ΔN + T680A mutant (**d**), stimulated by 10 mM camphor, 300 mM 2-APB or thermal stimulus + 10 mM 2-APB. **e**, Current densities (pA pF⁻¹) of HEK293 cells expressing mTRPV3-ΔN or mTRPV3-ΔN + T680A mutant, stimulated by heat, 10 mM camphor or 300 μM 2-APB. Graphs show mean and s.e.m. for indicated number of recordings. Source data are available online. **f**, Surface expression profiles of TRPV3 constructs with GFP. Western blotting with a GFP antibody, showing that the biotinylated samples incubated with and without beads include the targets, indicating that the TRPV3 mutant and wildtype are expressed on the cell surface.

6DVZ) (Extended Data Fig. 7e). These observations suggest that this lipid stabilizes the position of the S5 helix, thereby facilitating the hydrogen bond formation between Asp586 on S5 and Thr680 on S6, to contribute to the formation of the π-helical region of S6. These structures provide insights into the role of the lipid binding in maintaining the π-helical region of S6 (Fig. 5b).

A recent structural study suggested the molecular mechanism for heat-activated gating in TRPV3 (ref. 22). In this process, heat stimuli induce the conformational change of the ankyrin repeat domain, which consequently causes the structural change of the transmembrane domain. Although the role of lipids in the thermo-sensitization has not been elucidated in the previous study²², the lipid displacement

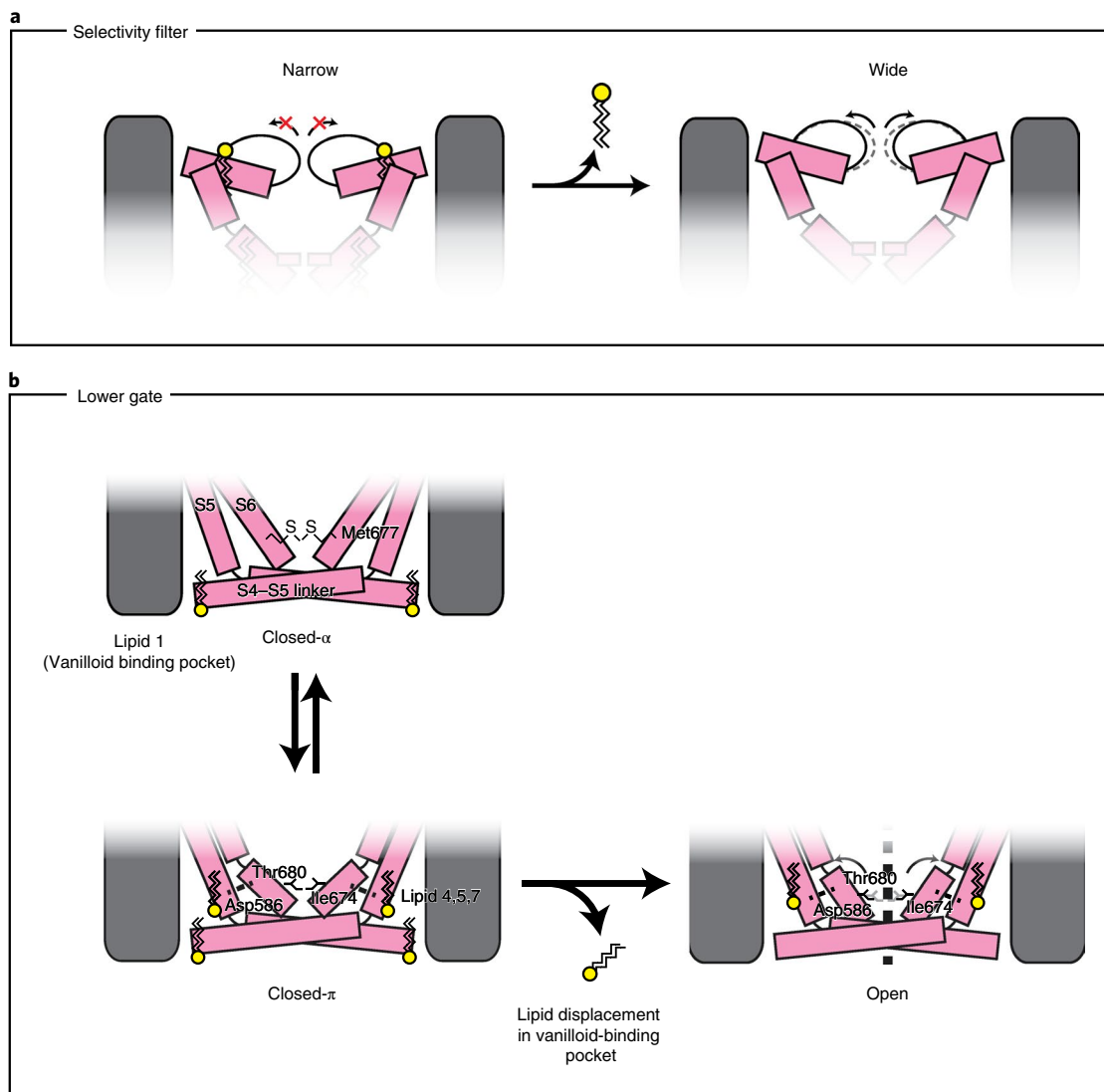


Fig. 5 | Proposed mechanistic models for TRPV3 activation. **a**, Speculative mechanism for the opening of the upper gate in TRPV3. The lipid between the S6 helix and pore helix (lipid 3) may be displaced on the widening of the selectivity filter. **b**, Speculative mechanism for the opening of the lower gate. The left two states represent the distinct closed states, the closed- α and closed- π states, and the right model represents the open state. TRPV3 adopts the closed- π state, rather than the closed- α state, in lipid bilayers. As speculated in previous structural studies of TRPV1, lipid displacement in the vanilloid-binding pocket may also be involved in the opening of TRPV3.

might be involved in the structural transitions from the closed- π to open state during the activation of TRPV3.

Online content

Any methods, additional references, Nature Research reporting summaries, source data, extended data, supplementary information, acknowledgements, peer review information; details of author contributions and competing interests; and statements of data and code availability are available at <https://doi.org/10.1038/s41594-020-0439-z>.

Received: 29 November 2019; Accepted: 24 April 2020;

Published online: 22 June 2020

References

- Ramsey, I. S., Delling, M. & Clapham, D. E. An introduction to Trp channels. *Ann. Rev. Physiol.* **68**, 619–647 (2005).
- Smith, G. D. et al. TRPV3 is a temperature-sensitive vanilloid receptor-like protein. *Nature* **418**, 186–190 (2002).
- Xu, H. et al. TRPV3 is a calcium-permeable temperature-sensitive cation channel. *Nature* **418**, 181–186 (2002).
- Sherkheli, M. A., Vogt-Eisele, A. K., Weber, K. & Hatt, H. Camphor modulates TRPV3 cation channels activity by interacting with critical pore-region cysteine residues. *Pak. J. Pharm. Sci.* **26**, 431–438 (2013).
- Chung, M.-K. 2-Aminoethoxydiphenyl borate activates and sensitizes the heat-gated ion channel TRPV3. *J. Neurosci.* **24**, 5177–5182 (2004).
- Vogt-Eisele, A. K. et al. Monoterpene agonists of TRPV3. *Br. J. Pharmacol.* **151**, 530–540 (2007).
- Qu, Y., Wang, G., Sun, X. & Wang, K. Inhibition of the warm-temperature activated Ca²⁺-permeable transient receptor potential vanilloid TRPV3 channel attenuates atopic dermatitis. *Mol. Pharmacol.* **96**, 393–400 (2019).
- Lin, Z. et al. Exome sequencing reveals mutations in TRPV3 as a cause of Olmsted syndrome. *Am. J. Hum. Genet.* **90**, 558–564 (2012).
- Atherton, D. J., Sutton, C. & Jones, B. M. Mutilating palmoplantar keratoderma with periorificial keratotic plaques (Olmsted's syndrome). *Br. J. Dermatol.* **122**, 245–252 (1990).
- Asakawa, M. et al. Association of a mutation in TRPV3 with defective hair growth in rodents. *J. Invest. Dermatol.* **126**, 2664–2672 (2006).
- Klein, A. S., Tannert, A. & Schaefer, M. Cholesterol sensitises the transient receptor potential channel TRPV3 to lower temperatures and activator concentrations. *Cell Calcium* **55**, 59–68 (2014).

12. Hu, H.-Z. et al. Potentiation of TRPV3 channel function by unsaturated fatty acids. *J. Cell. Physiol.* **208**, 201–212 (2006).
13. Doerner, J. F., Hatt, H. & Ramsey, I. S. Voltage- and temperature-dependent activation of TRPV3 channels is potentiated by receptor-mediated PI(4,5)P₂ hydrolysis. *J. Gen. Physiol.* **137**, 271–288 (2011).
14. Gao, Y., Cao, E., Julius, D. & Cheng, Y. TRPV1 structures in nanodiscs reveal mechanisms of ligand and lipid action. *Nature* **534**, 347–351 (2016).
15. Cao, E., Liao, M., Cheng, Y. & Julius, D. TRPV1 structures in distinct conformations reveal activation mechanisms. *Nature* **504**, 113–118 (2013).
16. Zubcevic, L. et al. Cryo-electron microscopy structure of the TRPV2 ion channel. *Nat. Struct. Mol. Biol.* **23**, 180–186 (2016).
17. Liao, M., Cao, E., Julius, D. & Cheng, Y. Structure of the TRPV1 ion channel determined by electron cryo-microscopy. *Nature* **504**, 107–112 (2013).
18. Singh, A. K., McGoldrick, L. L. & Sobolevsky, A. I. Structure and gating mechanism of the transient receptor potential channel TRPV3. *Nat. Struct. Mol. Biol.* **25**, 805–813 (2018).
19. Zubcevic, L. et al. Conformational ensemble of the human TRPV3 ion channel. *Nat. Commun.* **9**, 4773 (2018).
20. Zubcevic, L., Borschel, W. F., Hsu, A. L., Borgnia, M. J. & Lee, S. Y. Regulatory switch at the cytoplasmic interface controls TRPV channel gating. *Elife* **8**, e47746 (2019).
21. Liu, B., Yao, J., Zhu, M. X. & Qin, F. Hysteresis of gating underlies sensitization of TRPV3 channels. *J. Gen. Physiol.* **138**, 509–520 (2011).
22. Singh, A. K. et al. Structural basis of temperature sensation by the TRP channel TRPV3. *Nat. Struct. Mol. Biol.* **26**, 994–998 (2019).
23. Liu, B. & Qin, F. Single-residue molecular switch for high-temperature dependence of vanilloid receptor TRPV3. *Proc. Natl Acad. Sci. USA* **114**, 1589–1594 (2017).
24. Grandl, J. et al. Pore region of TRPV3 ion channel is specifically required for heat activation. *Nat. Neurosci.* **11**, 1007–1013 (2008).
25. Bayburt, T. H. & Sligar, S. G. Membrane protein assembly into nanodiscs. *FEBS Lett.* **584**, 1721–1727 (2010).
26. Chen, Q. et al. Structure of mammalian endolysosomal TRPML1 channel in nanodiscs. *Nature* **550**, 415–418 (2017).
27. Cheng, Y. et al. Structure of the human TRPM4 ion channel in a lipid nanodisc. *Science* **359**, 228–232 (2017).
28. Grinkova, Y. V., Denisov, I. G. & Sligar, S. G. Engineering extended membrane scaffold proteins for self-assembly of soluble nanoscale lipid bilayers. *Protein Eng. Des. Sel.* **23**, 843–848 (2010).
29. Smart, O. S., Neduvilil, J. G., Wang, X., Wallace, B. A. & Sansom, M. S. P. HOLE: a program for the analysis of the pore dimensions of ion channel structural models. *J. Mol. Graph.* **14**, 354–360 (1996).
30. Deng, Z. et al. Cryo-EM and X-ray structures of TRPV4 reveal insight into ion permeation and gating mechanisms. *Nat. Struct. Mol. Biol.* **25**, 252–260 (2018).
31. Tang, L. et al. Structural basis for Ca²⁺ selectivity of a voltage-gated calcium channel. *Nature* **505**, 56–61 (2014).
32. Shannon, R. D. Revised effective ionic radii and systematic studies of interatomic distances in halides and chalcogenides. *Acta Crystallogr. A Found. Adv.* **32**, 751–767 (1976).
33. Nightingale, E. R. Phenomenological theory of ion solvation. Effective radii of hydrated ions. *J. Phys. Chem.* **63**, 1381–1387 (1959).
34. Cheng, W. et al. Heteromeric heat-sensitive transient receptor potential channels exhibit distinct temperature and chemical response. *J. Biol. Chem.* **287**, 7279–7288 (2012).
35. Jara-Oseguera, A., Huffer, K. E. & Swartz, K. J. The ion selectivity filter is not an activation gate in TRPV1-3 channels. *Elife* **8**, e51212 (2019).

Publisher's note Springer Nature remains neutral with regard to jurisdictional claims in published maps and institutional affiliations.

This is a U.S. government work and not under copyright protection in the U.S.; foreign copyright protection may apply 2020

Methods

Protein expression and purification. The gene encoding the mouse TRPV3 type protein (UniprotKB Q8K424), lacking the flexible N-terminal region (residues 1–117), was cloned from mouse brain complementary DNA (ZYAGEN) into the pEG BacMam vector, with an N-terminal 8× His tag, maltose-binding protein and a tobacco etch virus (TEV) cleavage site, and expressed in HEK293 GnTI (*N*-acetylglucosaminyltransferase I-negative) cells (American Type Culture Collection, catalog no. CRL-3022) using the BacMam system (Thermo Fisher Scientific)³⁶. The baculovirus was generated in Sf9 cells (Life Technologies) following the standard protocol and used to infect HEK293 GnTI- cells at a ratio of 1 to 10 (virus HEK293, v/v). The infected cells were cultured in suspension at 37°C for 20 h and supplemented with 10 mM sodium butyrate to boost protein expression. The cells were then cultured in suspension at 37°C for 24 h, collected by centrifugation (6,000g, 10 min, 4°C) and disrupted by sonication in buffer A (20 mM HEPES-NaOH, pH 7.4, 200 mM NaCl) supplemented with 5.2 µg ml⁻¹ aprotinin, 2 µg ml⁻¹ leupeptin and 1.4 µg ml⁻¹ pepstatin A (all from Calbiochem). Cell debris was removed by centrifugation (10,000g, 10 min, 4°C). The membrane fraction was collected by ultracentrifugation (138,000g, 1 h, 4°C) and solubilized for 1 h at 4°C in buffer S (20 mM HEPES-NaOH, pH 7.4, 200 mM NaCl, 10% (v/v) glycerol, 2 mM tris(2-carboxyethyl)phosphine(TCEP)-NaOH (pH 7.4) 1% N-dodecyl-β-D-maltoside (DDM) (Calbiochem)). Insoluble materials were removed by ultracentrifugation (138,000g, 1 h, 4°C). The detergent-soluble fraction was incubated with amylose resin (New England Biolabs), equilibrated with SEC buffer (20 mM HEPES-NaOH (pH 7.4), 200 mM NaCl, 2 mM TCEP- NaOH (pH 7.4)) for 30 min at 4°C. The beads were washed with buffer (20 mM HEPES-NaOH, pH 7.4, 200 mM NaCl, 10% (v/v) glycerol, 2 mM tris(2-carboxyethyl)phosphine (TCEP)-NaOH (pH 7.4), 10 µg ml⁻¹ L-α-phosphatidylcholine (Soy) (SoyPC) (Avanti), 0.025% DDM (Calbiochem)). The protein sample was then eluted with 20 mM HEPES-NaOH, pH 7.4, 200 mM NaCl, 10% (v/v) glycerol, 2 mM TCEP-NaOH, (pH 7.4), 0.025% DDM (Calbiochem), 100 µg ml⁻¹ SoyPC and 20 mM maltose. The peak fractions were collected and concentrated to 2 mg ml⁻¹ for nanodisc reconstitution.

Nanodisc reconstitution and electron microscopy-grid preparation.

Concentrated MBP-TRPV3 was reconstituted into lipid nanodiscs, according to the published protocol¹⁴.

Before reconstitution, 10 mg SoyPC, dissolved in chloroform, was dried using a nitrogen stream and the residual chloroform was further removed by vacuum desiccation (O/N). Lipids were then rehydrated in buffer S, resulting in a clear 10 mM lipid stock. MSP2N2 was purified in-house and concentrated to 5.7 mg ml⁻¹.

In brief, TRPV3, MSP2N2 and SoyPC were mixed at a molar ratio of 1:4:200, respectively, and incubated on ice for 30 min. Detergents were removed by adding Bio-Beads SM2 (Bio-Rad) to 40 mg ml⁻¹, followed by gentle agitation. The Bio-Beads were replaced with fresh ones every 2 h, twice in total. The third batch of Bio-Beads (equal amount), together with TEV protease (1 mg TEV protease per 1 mg TRPV3), was then added and the sample was incubated at 4°C overnight. The Bio-Beads were then removed by passage through a PolyPrep column (Bio-Rad), and the lysate was ultracentrifuged (106,000g) before size-exclusion chromatography. Ultracentrifuged samples were purified by size-exclusion chromatography on a Superose 6 Increase 10/300 GL column (GE Healthcare), equilibrated with SEC buffer. The peak fractions of the protein were collected and concentrated to an absorbance (A_{280}) of 2.0, using a centrifugal filter unit (Merck Millipore, 100 kDa molecular weight cutoff). A 3 µl portion of the concentrated TRPV3 in a nanodisc was applied to a glow-discharged Quantifoil R1.2/1.3 Cu/Rh 300 mesh grid (Quantifoil), which was blotted using a Vitrobot Mark IV (FEI) under 6°C and 100% humidity conditions and then plunged into liquid ethane.

Electron microscopy image acquisition. The grid images were obtained with a Titan Krios transmission electron microscope (Thermo Fisher Scientific) operated at 300 kV, and recorded by a Falcon-III direct electron detector (Thermo Fisher Scientific) operated in the counting mode with a physical pixel size of 0.8346 Å. The data set was acquired with the EPU software (Thermo Fisher Scientific). Each image was dose-fractionated to 60 frames at a dose rate of 0.8–1.0 e⁻ per pixel per second, to accumulate a total dose of ~50 e⁻ Å⁻². In total, 1,818 counting mode movies were collected (Table 1).

Data processing and model building. Motion correction was performed with MotionCor2 (ref. ³⁷). Defocus parameters were estimated using CTFFIND 4.1 (ref. ³⁸). First, template-based auto-picking was performed with the two-dimensional class averages of a few hundred manually picked particles as templates. A total of 469,323 particles were extracted in 3.15 Å per pixel. These particles were divided into four batches and subjected to three rounds of two-dimensional classification in RELION 3.0 (ref. ^{39,40}). The initial model was generated in RELION. Subsequently, 254,758 good particles were further three-dimensionally classified in C4 symmetry. We also performed the three-dimensional classification without the symmetry using the selected 254,758 particles, and the result showed a similar four-fold symmetry of TRPV3. Finally, 106,947 particles in the classes were re-extracted in 1.15 Å per pixel and refined in C4 symmetry. The overall gold-standard resolution was 3.3 Å, with

the local resolution in the core transmembrane region extending to 2.9 Å and that in the peripheral region extending to 4.0 Å (Extended Data Fig. 2c,d).

The extracellular, transmembrane and intracellular regions of TRPV3 in a nanodisc were built into the density map in COOT⁴¹, using the TRPV3 in digitonin micelles (PDB 6DVW) structure as a guide. The initial model was then refined, using PHENIX⁴² with secondary structure restraints.

Cell culture for electrophysiology. HEK293T-derived cells were maintained at 37°C in a 5% CO₂ atmosphere in Dulbecco's modified Eagle's Medium (WAKO Pure Chemical Industries), containing 10% fetal bovine serum (Biowest SAS), 100 units per ml penicillin (Invitrogen Corp.), 100 µg ml⁻¹ streptomycin (Invitrogen Corp.) and 2 mM GlutaMAX (Invitrogen Corp.). For patch-clamp recordings, 1 µg wildtype, truncated N-terminal (ΔN), T680A mouse TRPV3 in the pEG BacMam vector and 0.1 µg pGreen Lantern 1 complementary DNA were used to transfet HEK293T cells cultured in 35 mm dishes, using the Lipofectamine Plus Reagent (Invitrogen Corp.). After an incubation for 3–4 h, the cells were reseeded on coverslips and further incubated at 33°C in 5% CO₂. Patch-clamp recordings were performed 1 d after transfection.

Chemicals for electrophysiology. The 2-aminoethoxydiphenyl borate (2-APB) was purchased from Sigma-Aldrich, and camphor was purchased from WAKO Chemicals. The 2-APB was dissolved in DMSO to prepare a stock solution (1 M), and the camphor was dissolved in ethanol as a stock solution (3 M) and then diluted to the final concentration using bath solution.

Electrophysiology. For whole-cell experiments, the experimental solutions were: (1) bath solution, 140 mM NaCl, 5 mM KCl, 2 mM MgCl₂, 5 mM EGTA, 10 mM HEPES and 10 mM glucose, at pH 7.4 adjusted with NaOH; and (2) pipette solution, 140 mM CsCl, 5 mM EGTA and 10 mM HEPES at pH 7.4, adjusted with CsOH. Data from whole-cell voltage-clamp recordings were acquired at 10 kHz throughout the experiments and filtered at 5 kHz for analysis (Axon 200B amplifier with pCLAMP software, Axon Instruments). The membrane potential was clamped at -60 mV.

All experiments were performed at 25°C, unless otherwise stated. Heat stimulation was induced by increasing the bath temperature, using a preheated solution warmed in an inline heater (1 °C s⁻¹, with a maximum of 40 or 55 °C). The temperature was monitored using a thermocouple (TC-344; Warner Instruments) placed within 100 µm of the patch-clamped cell. The heat stimulation was stopped on confirming that the TRPV3 currents were desensitized or inactivated. Temperature profiles and Arrhenius plots for the data from the whole-cell voltage-clamp recordings were calculated using the Origin software (OriginLab). The absolute current values were plotted on a log scale against the reciprocal of the absolute temperature (T) (Arrhenius plot), and the temperature threshold for channel activation was determined by the temperature that caused a change in the slope. For the current density analysis of TRPV3 channels, the peak currents induced by heat stimulation and chemical stimulation were measured and presented as pA pF⁻¹.

Plasma membrane and protein biotinylation. HEK293T cells were transfected with 1 µg plasmid DNA and incubated overnight at 33°C. The HEK293T cells were washed three times with PBS and incubated twice with 0.5 mg ml⁻¹ EZ-Link NHS-LC-Biotin (Abcam) for 10 min each. The cells were washed three times with quenching buffer (100 mM glycine in PBS, pH 7.3) and then washed with PBS. The cells were collected and lysed in RIPA buffer (Thermo Fisher) containing complete protease inhibitor cocktail (lysis buffer). Biotinylated proteins were precipitated overnight using 10 µl Dynabeads Myone Streptavidin T1 (Thermo Fisher Scientific) with agitation at 4°C. The beads were washed three times with 100 µl lysis buffer at room temperature. The beads (10 µl) and eluates were mixed with 2× Laemmli Sample Buffer (Bio-Rad) and 100 mM BME and heated at 95°C for 5 min, before resolution on an 8% SDS-PAGE gel. Samples were analyzed by western blotting.

Western blotting. For western blot experiments, gel electrophoresis was performed at 120 mV for 1.5 h. The proteins on the SDS-PAGE gel were transferred to a mini format, 0.45 µm polyvinyl difluoride membrane, using a Trans-Blot Turbo (Bio-Rad) at 120 mV for 3 h. Nonspecific sites were blocked by incubating the membrane in PBS-T containing 2% BSA. Primary antibodies (antigreen fluorescent protein (-GFP) IgG rabbit (MBL); diluted 1/500 in PBS-T containing 1% BSA) were incubated with the membrane overnight. The secondary antibody was incubated with the membrane for 1 h (anti-rabbit IgG HRP (Cell Signaling Technology); diluted 1/1,000 in PBS-T containing 1% BSA).

Statistical analysis. Data in all figures are shown as means ± s.e.m. Statistical analysis was conducted using analysis of variance (one-way analysis of variance) with Bonferroni correction, using the Origin 8.5 software. P values of <0.05 were considered statistically significant.

Reporting Summary. Further information on experimental design is available in the Nature Research Reporting Summary linked to this article.

Data availability

Cryo-EM density maps have been deposited in the Electron Microscopy Data Bank (EMDB), under accession number EMD-0882. Model coordinates have been deposited in the Protein Data Bank (wwPDB), under accession code PDB 6LGP. The associated electron microscopy data have been deposited in the Electron Microscopy Public Image Archive, under accession code EMPIAR-10400. Source data for Fig. 4e and Extended Data Fig. 1a are available with the paper online.

References

36. Dukkipati, A., Park, H. H., Waghray, D., Fischer, S. & Garcia, K. C. BacMam system for high-level expression of recombinant soluble and membrane glycoproteins for structural studies. *Protein Expr. Purif.* **62**, 160–170 (2008).
37. Zheng, S. Q. et al. MotionCor2: anisotropic correction of beam-induced motion for improved cryo-electron microscopy. *Nat. Methods* **14**, 331–332 (2017).
38. Rohou, A. & Grigorieff, N. CTFFIND4: fast and accurate defocus estimation from electron micrographs. *J. Struct. Biol.* **192**, 216–221 (2015).
39. Zivanov, J. et al. New tools for automated high-resolution cryo-EM structure determination in RELION-3. *Elife* **7**, e42166 (2018).
40. Zivanov, J., Nakane, T. & Scheres, S. H. W. A Bayesian approach to beam-induced motion correction in cryo-EM single-particle analysis. *IUCrJ* **6**, 5–17 (2019).
41. Emsley, P. & Cowtan, K. Coot: model-building tools for molecular graphics. *Acta Crystallogr. D Biol. Crystallogr.* **60**, 2126–2132 (2004).
42. Afonine, P. V. et al. Real-space refinement in PHENIX for cryo-EM and crystallography. *Acta Crystallogr. D Struct. Biol.* **74**, 531–544 (2018).

Acknowledgements

We thank T. Nakane for computational support and assistance with the single-particle analysis and model building, K. Yamashita for computational support and model building and Y. Lee for fruitful discussions and encouragement. We also thank the staff scientists at the University of Tokyo's cryo-EM facility, especially K. Kobayashi,

H. Yanagisawa, A. Tsutsumi, M. Kikkawa and R. Danev. This work was supported by a MEXT Grant-in-Aid for Specially Promoted Research (grant no. 16H06294) to O.N. and by MEXT KAKENHI Grant-in-Aid for Scientific Research(C) (18K60156). This research was supported by the Platform Project for Supporting Drug Discovery and Life Science Research (Basis for Supporting Innovative Drug Discovery and Life Science Research) from AMED under grant no. JP19am01011115 (support number 1110).

Author contributions

H.S., T.K., T.H. and O.N. designed the project. T.K. investigated the conditions for TRPV3 expression. H.S. performed protein expression, purification and cryo-EM sample preparation, with assistance from T.K. H.S., T.K. and T.N. performed data collection. H.S. processed and analyzed the cryo-EM data with assistance from T.K. T.N., H.S. and T.K. built the models. T.H.D.N. and M.T. performed the electrophysiology, protein biotinylation, western blotting and statistical analysis. H.S., T.K., T.H.D.N., T.N., T.H., M.T. and O.N. wrote the manuscript. O.N. supervised the research.

Competing interests

The authors declare no competing interests.

Additional information

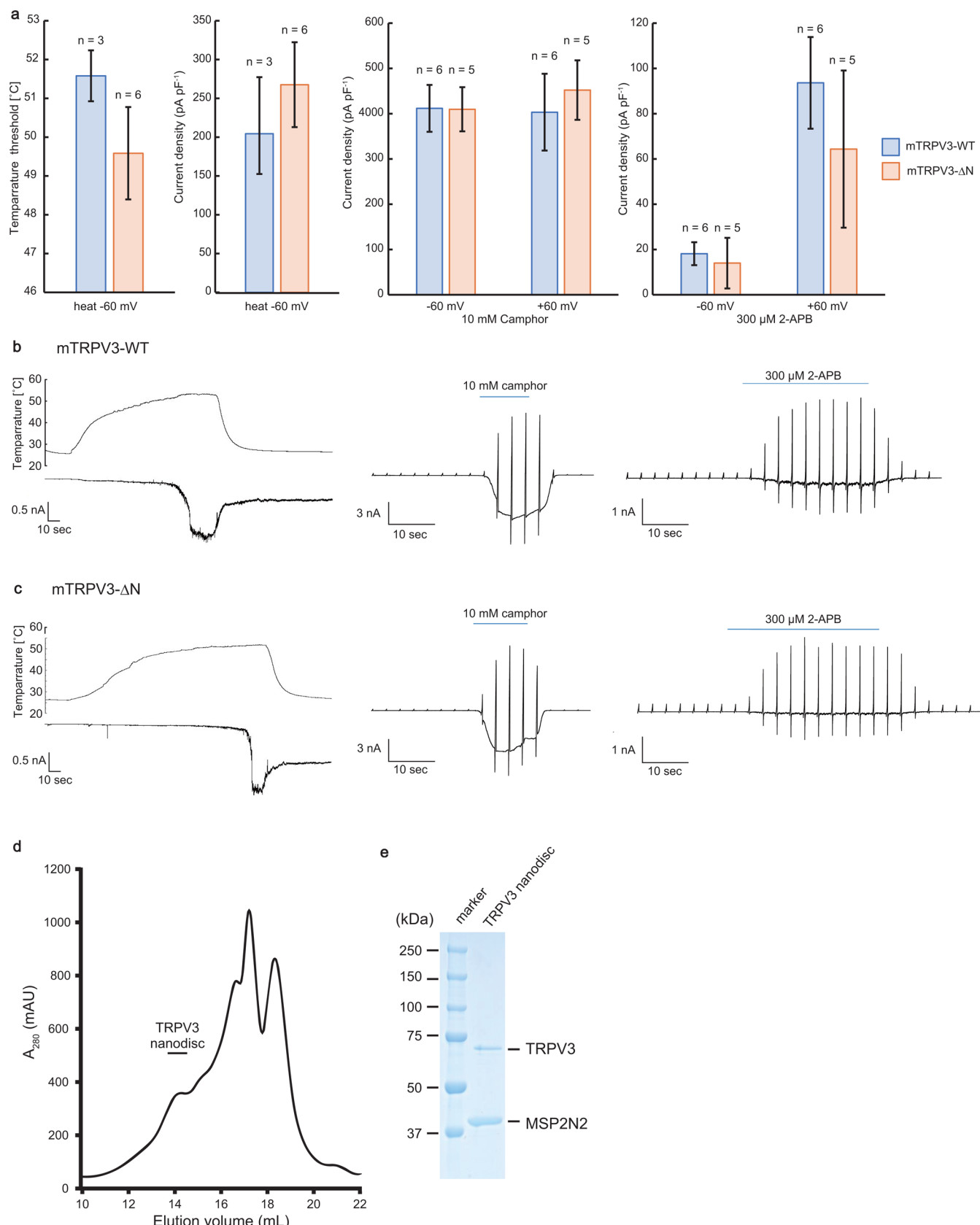
Extended data is available for this paper at <https://doi.org/10.1038/s41594-020-0439-z>.

Supplementary information is available for this paper at <https://doi.org/10.1038/s41594-020-0439-z>.

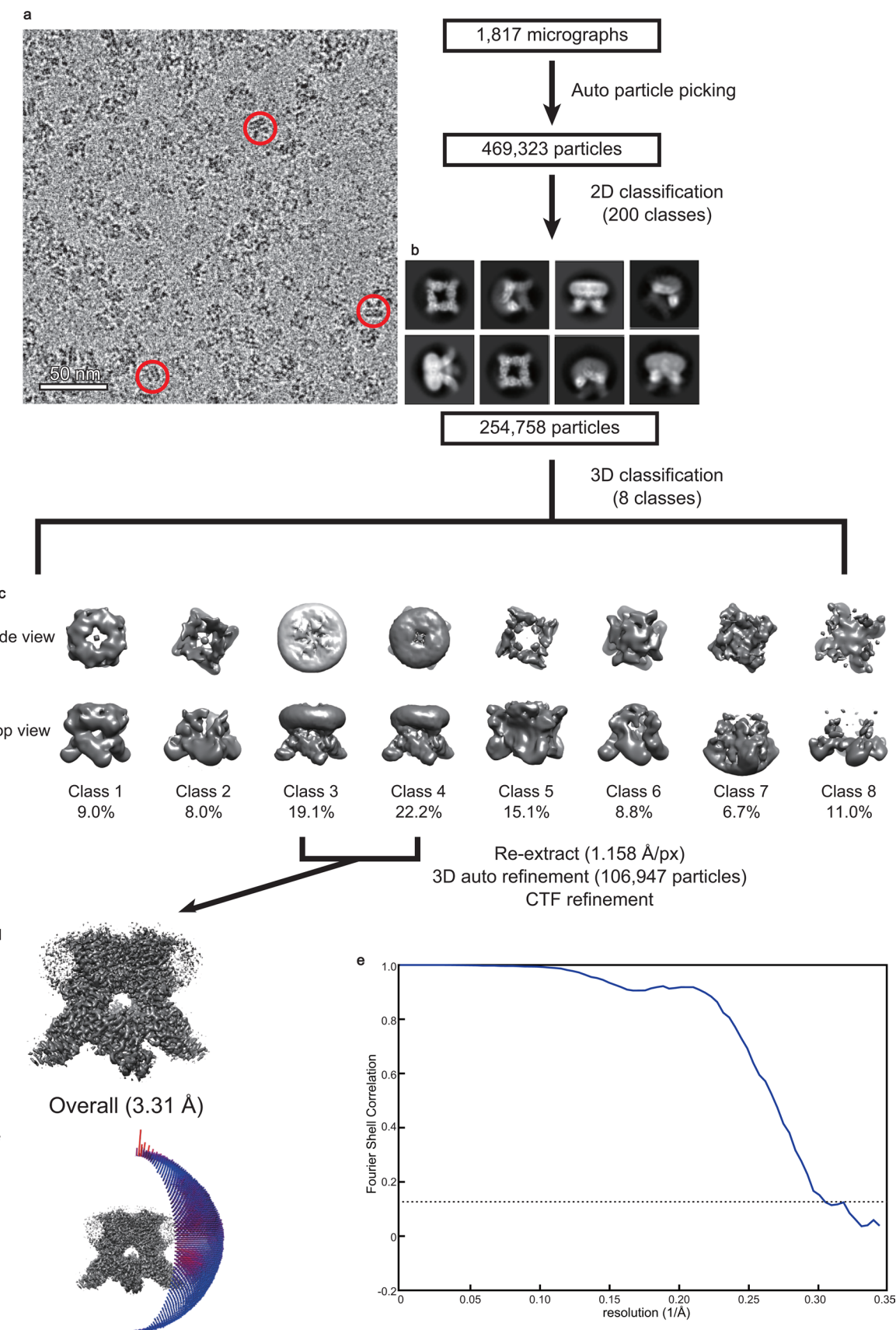
Correspondence and requests for materials should be addressed to O.N.

Peer review information Katarzyna Marcinkiewicz was the primary editor on this article and managed its editorial process and peer review in collaboration with the rest of the editorial team.

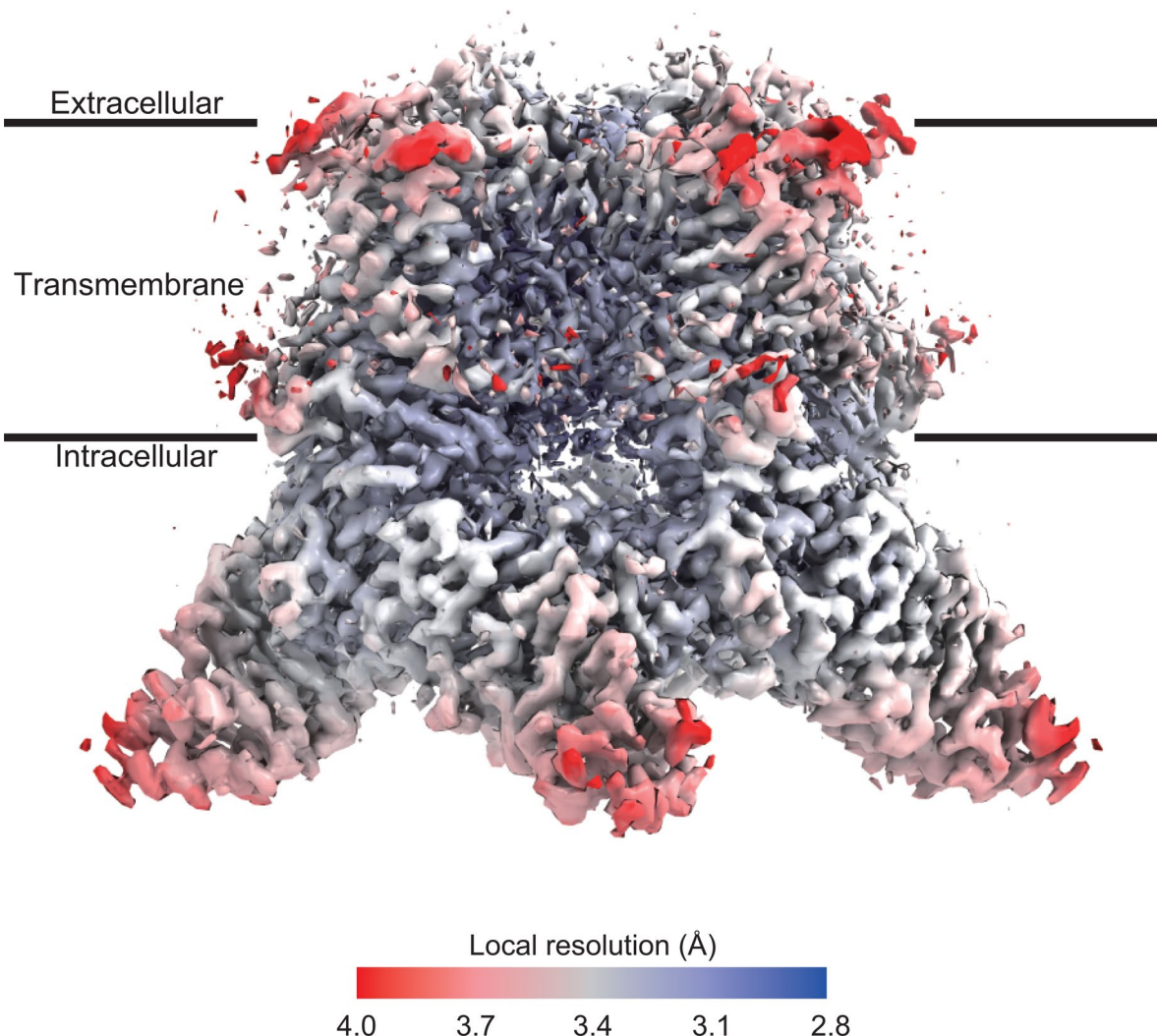
Reprints and permissions information is available at www.nature.com/reprints.



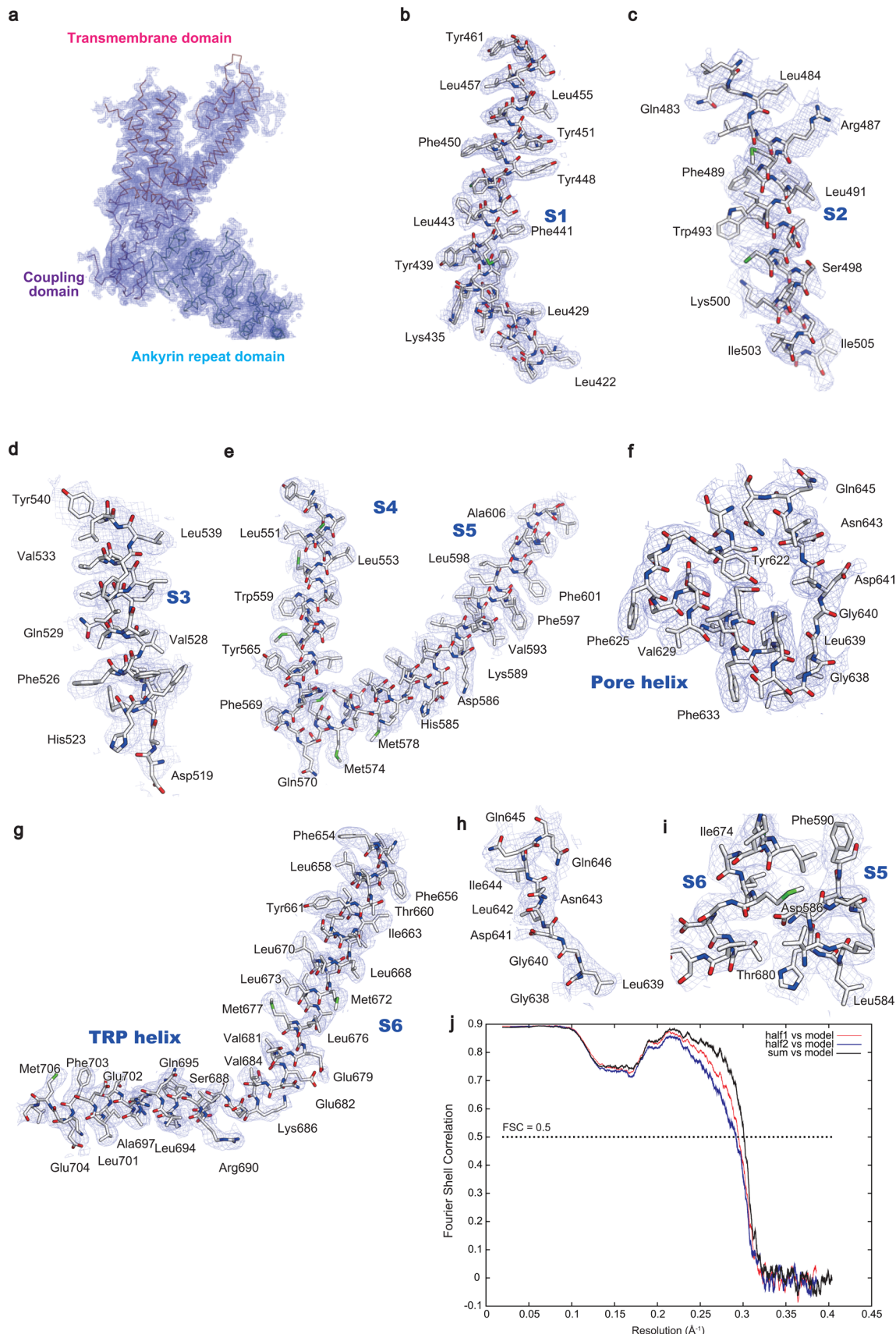
Extended Data Fig. 1 | Functional characterization and nanodisc reconstitution of truncated mutant TRPV3. **a**, Temperature thresholds of mTRPV3WT (light blue) and mTRPV3-ΔN (light orange), stimulated by heat, 10 mM camphor, or 300 mM 2-APB. **b, c**, Electrophysiological comparison between mouse TRPV3 WT (mTRPV3-WT) (**b**) and N-terminal truncated mutant (mTRPV3-ΔN) (**c**), by whole-cell patch-clamp recordings in HEK293 cells. mTRPV3-ΔN has the same electrophysiological profile as mTRPV3-WT. Graphs show mean and s.e.m. for indicated number of recordings. The source data are available online. **d, e**, Size exclusion chromatogram (**d**) and SDS-PAGE (**e**) of mTRPV3-ΔN in a nanodisc.



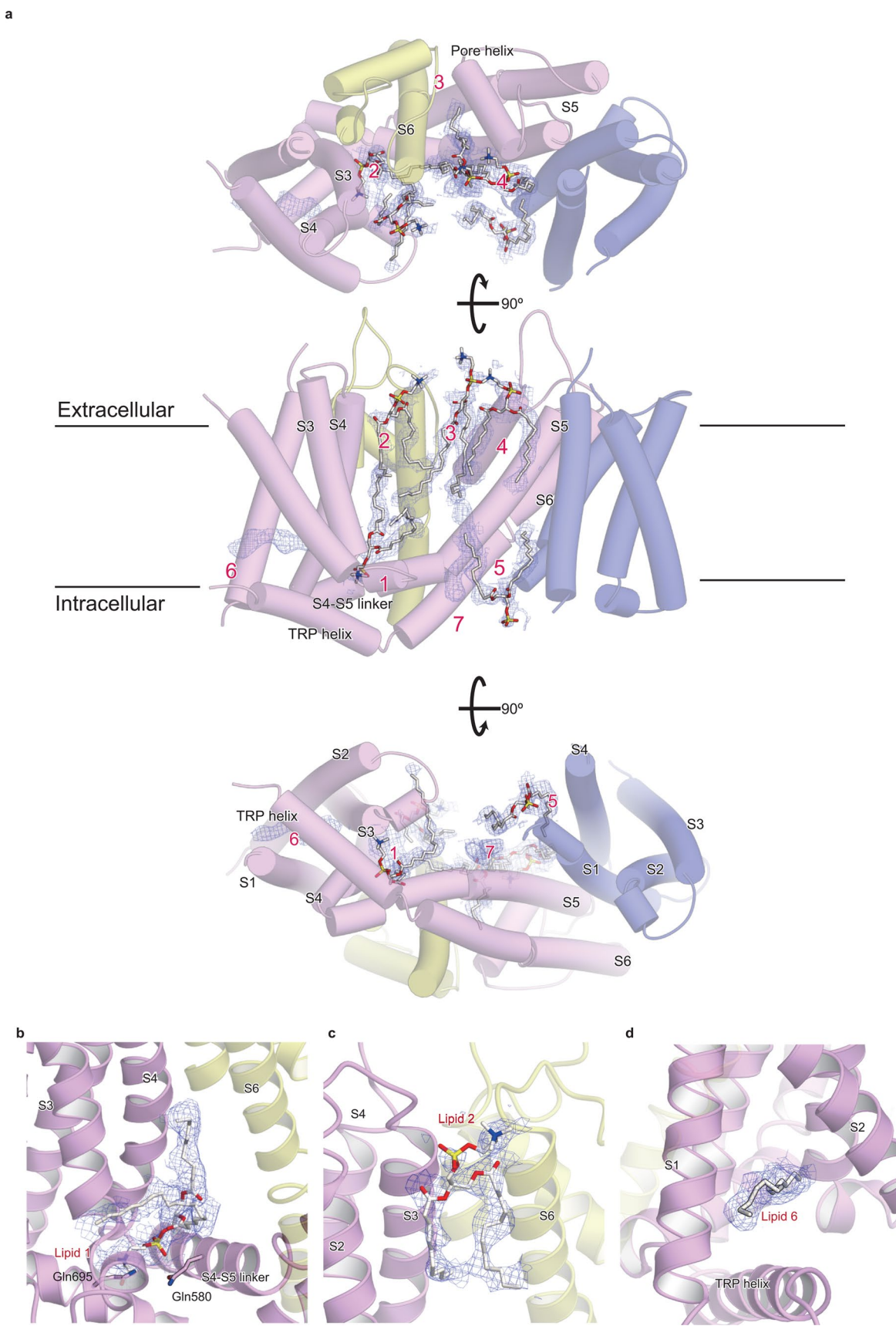
Extended Data Fig. 2 | Overview of single-particle cryo-EM for mTRPV3-ΔN in a nanodisc. **a**, Cryo-EM micrograph of mTRPV3-ΔN in a nanodisc, with example particles circled in red. **b**, Reference-free 2D class images of mTRPV3-ΔN in a nanodisc. **c**, 3D class averages of mTRPV3-ΔN in a nanodisc. **d**, Refined density, at 3.31 Å resolution ($FSC = 0.143$). **e**, FSC curves of the map of TRPV3 in a nanodisc. The horizontal dashed line indicated $FSC = 0.143$. **f**, Euler angular distribution for particles used in the final map of TRPV3 in a nanodisc.



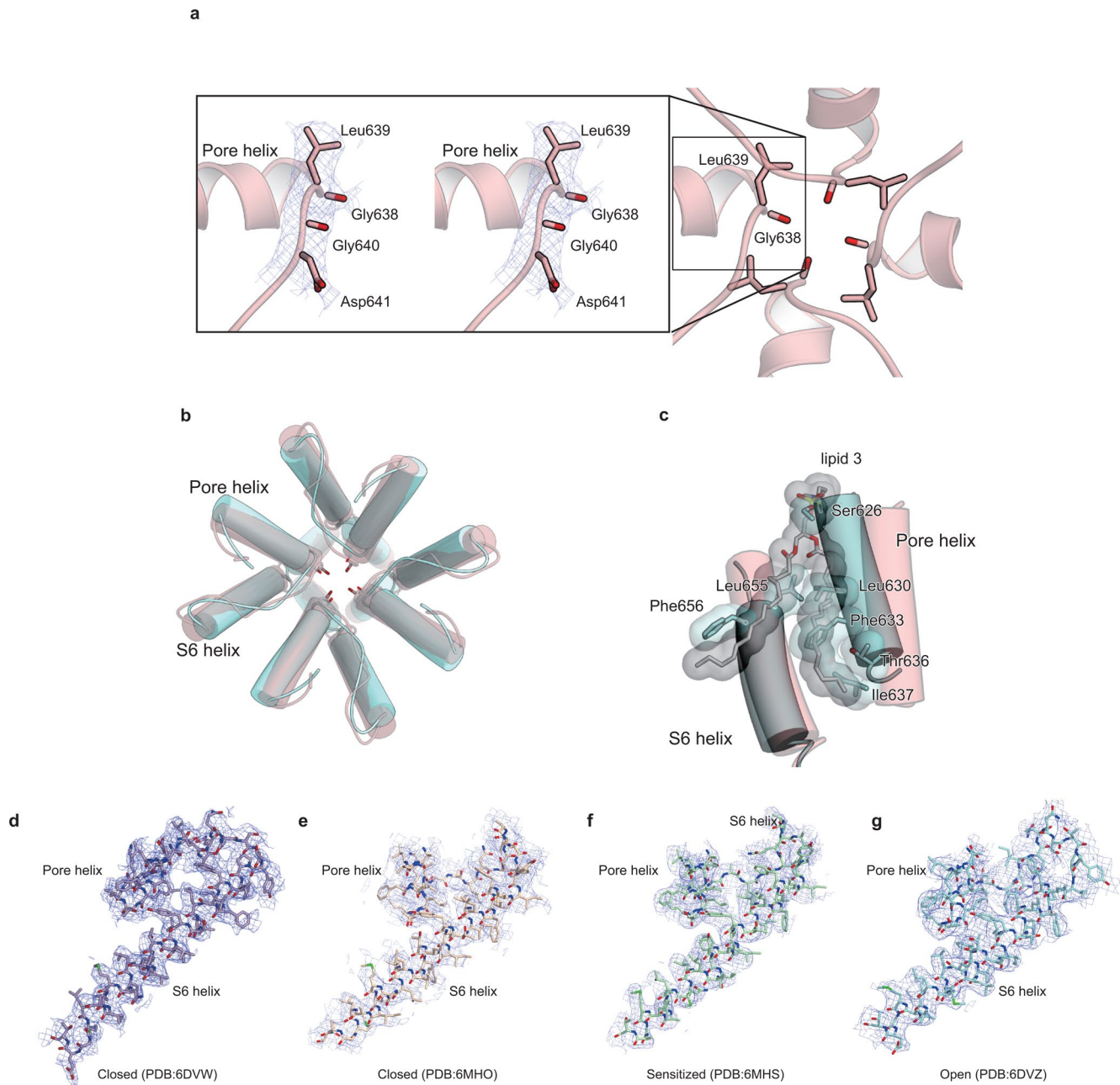
Extended Data Fig. 3 | The local resolution mapped on the density of mTRPV3- Δ N in a nanodisc. The map was obtained using CueMol2 at a 0.010 threshold level (<http://www.cuemol.org/>). The local resolution is higher in the Transmembrane core than the Intracellular region.



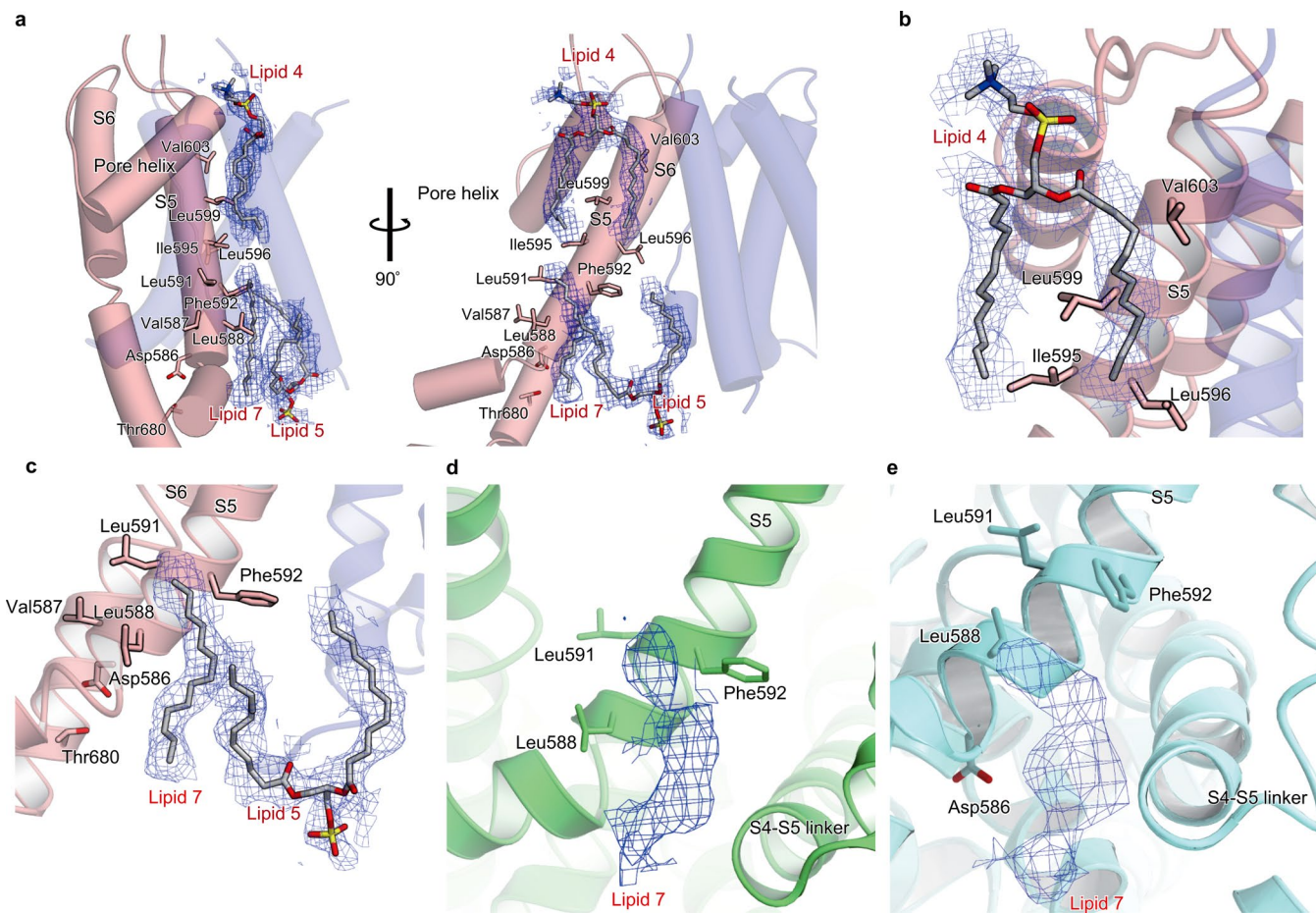
Extended Data Fig. 4 | Cryo-EM density of mTRPV3- Δ N in a nanodisc. **a**, Cryo-EM density (blue mesh) at 2.4σ for a single TRPV3 subunit; the structure, shown as a ribbon, is colored according to the domains. **b–i**, Fragments of the TRPV3 transmembrane region with the corresponding cryo-EM densities shown as a blue mesh at 2.4σ . **j**, Cross-validation FSC curves for the refined model versus unfiltered half maps (only half map 1 was used for refinement with PHENIX⁴²) and the summed map.



Extended Data Fig. 5 | Lipid-like densities observed in mTRPV3- Δ N in a nanodisc. **a**, The seven lipid-like densities (1-7) observed in mTRPV3- Δ N in a nanodisc map. Five densities (1-5) are sufficient to be modeled as phosphatidylcholine. The density is shown at 3.5σ . **b**, The site occupied by Lipid 1, known as the Vanilloid Binding Pocket, in TRPV1 structures in nanodiscs (PDB: 5IRZ). **c, d**, The lipid-like densities ascribed to Lipid 2 (c) and Lipid 6 (d) are observed in the TRPV3 structure in digitonin micelles (PDB: 6DVW).



Extended Data Fig. 6 | Model validation map of selectivity filter. **a**, Ribbon model around the selectivity filter, in stereo. The oxygens of the Gly638 and Gly640 mainchains, and the side chains of Leu639 and Asp641 are shown in stick models. EM density map around Gly638 - Asp641 shown in a gray mesh. **b**, Superimposition of the pore domain of TRPV3 in a nanodisc (pink) and the TRPV3 open state (light blue) (PDB: 6DVZ), according to the C α atoms of the S6 helices (Pro651-Ser685), viewed from the extracellular side (same perspective as Fig. 3a). **c**, Comparison of the phospholipid-binding site in Fig. 3c between TRPV3 in a nanodisc (pink) and the TRPV3 open state (light blue) (same perspective as Fig. 3d). Both models are superimposed on the C α atoms of the S6 helix (Pro651-Ser685) as a guide. The phospholipid observed in a nanodisc and the residues shown in Fig. 3c in the open state are indicated by stick and CPK models, respectively, revealing that the residues clashed with Lipid 3. **d-g**, Known TRPV3 structural models fitted to each EM density map (shown in blue mesh). TRPV3 in the closed state in digitonin micelles (purple) (**d**), closed state in amphipol (yellow) (**e**), sensitized state (green) (**f**), and open state (light blue) (**g**).



Extended Data Fig. 7 | Close-up views of Lipid 4, Lipid 5, and Lipid 7. **a**, Locations of the densities observed in Lipid 4, Lipid 5, and Lipid 7, indicated as a blue mesh at 3.0σ . The modeled phosphatidylcholine (Lipid 4, Lipid 5), the partially modeled acyl chain (Lipid 7), and the residues near Lipid 4 and Lipid 7 are shown as sticks. **b**, Interaction between Lipid 4 and the extracellular part of the S5 helix, viewed from the extracellular side and the residues nearby Lipid 4 are shown as sticks. **c**, Interactions among the intracellular region of the S5 helix, Lipid 5, and Lipid 7, viewed parallel to the membrane, and the residues nearby Lipid 7 are shown as sticks. **d**, **e**, Location of the density observed for Lipid 7 in previously reported structures: TRPV3-sensitized state (PDB: 6MHS) (**d**), TRPV3 open state (PDB: 6DVZ) (**e**), and the residues nearby the densities are shown as sticks.

Reporting Summary

Nature Research wishes to improve the reproducibility of the work that we publish. This form provides structure for consistency and transparency in reporting. For further information on Nature Research policies, see [Authors & Referees](#) and the [Editorial Policy Checklist](#).

Statistics

For all statistical analyses, confirm that the following items are present in the figure legend, table legend, main text, or Methods section.

n/a Confirmed

- The exact sample size (n) for each experimental group/condition, given as a discrete number and unit of measurement
- A statement on whether measurements were taken from distinct samples or whether the same sample was measured repeatedly
- The statistical test(s) used AND whether they are one- or two-sided
Only common tests should be described solely by name; describe more complex techniques in the Methods section.
- A description of all covariates tested
- A description of any assumptions or corrections, such as tests of normality and adjustment for multiple comparisons
- A full description of the statistical parameters including central tendency (e.g. means) or other basic estimates (e.g. regression coefficient) AND variation (e.g. standard deviation) or associated estimates of uncertainty (e.g. confidence intervals)
- For null hypothesis testing, the test statistic (e.g. F , t , r) with confidence intervals, effect sizes, degrees of freedom and P value noted
Give P values as exact values whenever suitable.
- For Bayesian analysis, information on the choice of priors and Markov chain Monte Carlo settings
- For hierarchical and complex designs, identification of the appropriate level for tests and full reporting of outcomes
- Estimates of effect sizes (e.g. Cohen's d , Pearson's r), indicating how they were calculated

Our web collection on [statistics for biologists](#) contains articles on many of the points above.

Software and code

Policy information about [availability of computer code](#)

Data collection

EPU, Clampex 10.7, Clampfit 10.7

Data analysis

MotionCorr2, RELION 3.0, Origin 8.1.J, HOLE, COOT, PHENIX, UCSF Chimera, CueMol2(<http://www.cuemol.org/>)

For manuscripts utilizing custom algorithms or software that are central to the research but not yet described in published literature, software must be made available to editors/reviewers. We strongly encourage code deposition in a community repository (e.g. GitHub). See the Nature Research [guidelines for submitting code & software](#) for further information.

Data

Policy information about [availability of data](#)

All manuscripts must include a [data availability statement](#). This statement should provide the following information, where applicable:

- Accession codes, unique identifiers, or web links for publicly available datasets
- A list of figures that have associated raw data
- A description of any restrictions on data availability

The atomic coordinate for the TRPV3 has been deposited in the Protein Data Bank, with the accession codes PDB 6LGP. Cryo-EM density map have been deposited in the Electron Microscopy Data Bank (EMDB) under accession numbers EMD-0882. The associated electron microscopy data have been deposited in the Electron Microscopy Public Image Archive, under accession code EMPIAR-10400.

Field-specific reporting

Please select the one below that is the best fit for your research. If you are not sure, read the appropriate sections before making your selection.

Life sciences Behavioural & social sciences Ecological, evolutionary & environmental sciences

For a reference copy of the document with all sections, see nature.com/documents/nr-reporting-summary-flat.pdf

Life sciences study design

All studies must disclose on these points even when the disclosure is negative.

Sample size	No sample size calculation was performed. The sample sizes were chosen in order to adequately reflect the variance in the measured effect.
Data exclusions	No samples or animals were excluded.
Replication	Replications were successful.
Randomization	N/A
Blinding	Not blinded.

Reporting for specific materials, systems and methods

We require information from authors about some types of materials, experimental systems and methods used in many studies. Here, indicate whether each material, system or method listed is relevant to your study. If you are not sure if a list item applies to your research, read the appropriate section before selecting a response.

Materials & experimental systems		Methods	
n/a	Involved in the study	n/a	Involved in the study
<input type="checkbox"/>	<input checked="" type="checkbox"/> Antibodies	<input checked="" type="checkbox"/>	<input type="checkbox"/> ChIP-seq
<input type="checkbox"/>	<input checked="" type="checkbox"/> Eukaryotic cell lines	<input checked="" type="checkbox"/>	<input type="checkbox"/> Flow cytometry
<input checked="" type="checkbox"/>	<input type="checkbox"/> Palaeontology	<input checked="" type="checkbox"/>	<input type="checkbox"/> MRI-based neuroimaging
<input checked="" type="checkbox"/>	<input type="checkbox"/> Animals and other organisms		
<input checked="" type="checkbox"/>	<input type="checkbox"/> Human research participants		
<input checked="" type="checkbox"/>	<input type="checkbox"/> Clinical data		

Antibodies

Antibodies used	Anti-GFP IgG rabbit polyclonal (MBL 598), Anti -rabbit IgG HRP-linked Antibody (Cell Signalling Technology 7074-S)
Validation	https://ruo.mbl.co.jp/bio/dtl/dtlfiles/598-v14.pdf , https://media.cellsignal.com/pdf/7074.pdf

Eukaryotic cell lines

Policy information about cell lines	
Cell line source(s)	Sf9, HEK293S GnT-I- (N-acetylglucosaminyl-transferase I-negative), HEK293T
Authentication	ATCC CRL-1711, ATCC CRL-3022, ATCC CRT-3216
Mycoplasma contamination	not tested
Commonly misidentified lines (See ICLAC register)	N/A